



Article

Scanning Near-Field Optical Microscopy of Ultrathin Gold Films

Dmitry I. Yakubovsky¹, Dmitry V. Grudin¹ , Georgy A. Ermolaev¹ , Andrey A. Vyshnevyy¹ , Mikhail S. Mironov¹, Sergey M. Novikov¹ , Aleksey V. Arsenin^{1,2} and Valentyn S. Volkov^{1,*}

¹ Center for Photonics and 2D Materials, Moscow Institute of Physics and Technology, 9 Institutsky Lane, Dolgoprudny 141700, Russia; dmitrii.yakubovskii@phystech.edu (D.I.Y.); grudin.dv@phystech.edu (D.V.G.); georgiy.ermolayev@phystech.edu (G.A.E.); andrey.vyshnevyy@phystech.edu (A.A.V.); mironov.ms@phystech.edu (M.S.M.); novikov.s@mipt.ru (S.M.N.); arsenin.av@mipt.ru (A.V.A.)
² Laboratory of Advanced Functional Materials, Yerevan State University, Yerevan 0025, Armenia
* Correspondence: vsv.mipt@gmail.com; Tel.: +7-926-735-93-98

Abstract: Ultrathin metal films are an essential platform for two-dimensional (2D) material compatible and flexible optoelectronics. Characterization of thin and ultrathin film-based devices requires a thorough consideration of the crystalline structure and local optical and electrical properties of the metal-2D material interface since they could be dramatically different from the bulk material. Recently, it was demonstrated that the growth of gold on the chemical vapor deposited monolayer MoS₂ leads to a continuous metal film that preserves plasmonic optical response and conductivity even at thicknesses below 10 nm. Here, we examined the optical response and morphology of ultrathin gold films deposited on exfoliated MoS₂ crystal flakes on the SiO₂/Si substrate via scattering-type scanning near-field optical microscopy (s-SNOM). We demonstrate a direct relationship between the ability of thin film to support guided surface plasmon polaritons (SPP) and the s-SNOM signal intensity with a very high spatial resolution. Using this relationship, we observed the evolution of the structure of gold films grown on SiO₂ and MoS₂ with an increase in thickness. The continuous morphology and superior ability with respect to supporting SPPs of the ultrathin (≤ 10 nm) gold on MoS₂ is further confirmed with scanning electron microscopy and direct observation of SPP fringes via s-SNOM. Our results establish s-SNOM as a tool for testing plasmonic films and motivate further theoretical research on the impact of the interplay between the guided modes and the local optical properties on the s-SNOM signal.

Keywords: ultrathin metal films; s-SNOM; MoS₂; surface plasmon polaritons; dielectric constants



Citation: Yakubovsky, D.I.; Grudin, D.V.; Ermolaev, G.A.; Vyshnevyy, A.A.; Mironov, M.S.; Novikov, S.M.; Arsenin, A.V.; Volkov, V.S. Scanning Near-Field Optical Microscopy of Ultrathin Gold Films. *Nanomaterials* **2023**, *13*, 1376. <https://doi.org/10.3390/nano13081376>

Academic Editor: Antonino Gulino

Received: 7 April 2023
Revised: 13 April 2023
Accepted: 13 April 2023
Published: 15 April 2023



Copyright: © 2023 by the authors. Licensee MDPI, Basel, Switzerland. This article is an open access article distributed under the terms and conditions of the Creative Commons Attribution (CC BY) license (<https://creativecommons.org/licenses/by/4.0/>).

1. Introduction

Ultrathin metal films are essential elements of novel optoelectronic, photonic, and plasmonic devices [1–3]. Thanks to their transparency, conductivity, and mechanical stability, gold, silver, or copper ultrathin films of thicknesses below 10 nm are a promising platform for developing flexible transparent electrodes in various optoelectronic applications [4,5]. For example, plasmonic waveguides, hyperbolic metamaterials, and transparent electrodes made from ultrathin films should possess smooth and continuous structural morphology to have a superior optical response and electronic properties [6–8]. To realize ultrathin film growth, the conventional three-dimensional (3D) mechanism in the Volmer-Weber regime [9] should be avoided by using special deposition conditions [10] or inserting additional wetting layers [11]. One of the competing methods to obtain continuous two-dimensional (2D) metal growth on a substrate is employing atomically thin two-dimensional (2D) underlayers, such as monolayer or few-layer graphene or transition metal dichalcogenide (TMD), which favors continuous metal growth kinetics [12–14]. Among them, molybdenum disulfide (MoS₂) has received large attention due to its tunable bandgap, high refractive index, and giant optical anisotropy resulting in a wide range of

applications from field-effect transistors to solar cells and photodetectors [15–19]. In this regard, investigation of Au/MoS₂ or other TMD interfaces is of great practical interest.

Recently, 2D MoS₂ layers demonstrated impressive results of gold ultrathin film growth. Due to the surface wetting effect and the adhesion of gold to MoS₂, high nucleation density and unusual kinetics of Au adatoms on MoS₂ surface lead to the growth of continuous and ultrasoft clusters and highly-percolated structures [13,20–22]. In recent papers, a detailed investigation of metal growth on MoS₂ revealed the formation of atomically flat Au clusters, nanotriangles, and nanoparticles depending on the deposition technique, metal thickness, and temperature [20,21,23–27]. For example, the presence of MoS₂ could enhance the performance of ultrathin noble metal electrodes and their optical response [22,25,28–30]. At the same time, the decoration of 2D MoS₂ layers with nanoparticles helps to control and improve the characteristics of transistors, photodetectors, and Raman sensors [23,31,32]. However, despite its great importance, there is still no detailed study of continuous ultrathin gold films grown on exfoliated MoS₂.

Investigation of the optical response of continuous gold films grown on small (~1 μm) flakes of MoS₂ and nanoscale structures via far-field optical techniques, such as spectroscopic ellipsometry and reflectometry, is challenging. Nevertheless, one can study the optical properties on the nanometer scale via scanning optical probe methods. Among them, s-SNOM is a powerful technique for probing the optical response in material with nanoscale resolution [33]. In particular, s-SNOM was successfully utilized for the characterization of thin films [34], nanoparticles [35,36], optoelectronic devices [37], surface enhanced Raman spectroscopy biosensors [38,39] and layered van der Waals materials, such as graphene and TMDs [40–42]. Furthermore, in plasmonics and photonics, s-SNOM is an effective tool for the excitation and detection of surface plasmon and phonon polaritons in layered structures [43]. The detected s-SNOM signal strongly depends on the optical response of the tip-sample interaction area, which governs the scattering efficiency of light by the tip [44,45]. As a result, the light scattering efficiency by the tip in the near-field is stronger on metal with a higher modulus of the real part of permittivity [46,47]. In practice, this results in a high contrast in s-SNOM amplitude and phase between the metal and dielectric areas of the sample, which are distinguishable with nanoscale spatial resolution [45,46]. This fact allows to perform mapping of the local homogeneity of dielectric permittivity of the material, analyze the quality of the sample morphology, and identify sub-diffraction features on the surface [45,48,49]. Our previous work demonstrated that, for ultrathin gold films grown on different 2D materials, the s-SNOM near-field intensity correlates well with their far-field dielectric response [50].

This study demonstrates the transformation of gold film morphology during growth on exfoliated MoS₂ flakes. Furthermore, morphological study with scanning electron and atomic-force microscopies was extended with s-SNOM near-field studies, which allowed to demonstrate of a qualitative improvement of plasmonic properties and structural evolution of metallic films on MoS₂, which is crucial for next-generation ultrathin metal optoelectronics.

2. Materials and Methods

For the deposition of gold films, MoS₂ 2D-crystal flakes were prepared via mechanical exfoliation on SiO₂/Si wafer using scotch tape and bulk MoS₂ crystal (2D semiconductors). To remove scotch residuals, the exfoliated flakes with substrates were carefully cleaned in acetone prior to deposition. Then, gold films were deposited via the electron-beam evaporation method in a high vacuum (~10⁻⁶ Torr) chamber setup (Nano-Master NEE-4000, Austin, TX, USA) at room temperature onto the prepared substrate of MoS₂ flakes/SiO₂. The mass-equivalent thicknesses of gold in the range of 4–10 nm and the deposition rate of ~1 Å/s were measured in-situ via a calibrated quartz-crystal sensor.

The crystal quality of MoS₂ flakes and the number of atomic layers in them were assessed by confocal Raman microscope Horiba LabRAM HR Evolution (Horiba Ltd., Kyoto, Japan). All measurements were carried out with laser excitation wavelengths of

632.8 nm with an 1800 lines/mm diffraction grating and a $\times 100$ (N.A. = 0.90) objective. The spot diameter was $\sim 0.5 \mu\text{m}$.

The structural morphology of the deposited Au films was visualized via scanning electron microscopy (SEM, JSM7001F, JEOL, Tokyo, Japan) working in the secondary electron imaging mode with a Schottky emitter, an acceleration voltage of 30 kV and a working distance of $\sim 6 \text{ mm}$. To characterize the surface roughness and homogeneity of films, we performed atomic force microscopy (AFM, Ntegra II, NT-MDT Spectrum Instruments, Moscow, Russia) working in the peak-force mode with a tip of radius $< 10 \text{ nm}$ and a resonant cantilever frequency of $\sim 140 \text{ kHz}$ (NT-MDT, ETALON, HA_NC).

Optical near-field characterization of Au films grown on MoS₂ flakes was performed using a scattering-type scanning near-field optical microscope (s-SNOM, neaSNOM, Neaspec GmbH, Haar, Germany) working in the reflection mode [46,47]. In this setup, we used a standard AFM tip coated with platinum, working in the tapping mode with a resonance frequency of $\Omega \approx 280 \text{ kHz}$. The s-SNOM tip was illuminated via a focused linearly polarized laser beam ($\lambda = 1550 \text{ nm}$) with an angle to the sample surface of about 50° . Next, the near-field was scattered by the tip interacting with the surface and redirected by an upper parabolic mirror to a highly sensitive photodetector. In addition, a pseudo-heterodyne interferometric scheme and demodulation of the detected scattered signal at higher harmonics (4Ω) were used for acquiring a near-field signal filtered from the background contribution.

3. Results and Discussion

First, few-layered MoS₂ flakes were located on the SiO₂ (285 nm)/Si substrate by their color contrast using an optical microscope. A typical optical image of the prepared flake with terraces consisting of a few MoS₂ layers is shown in Figure 1a. The crystal quality and the number of layers were determined via Raman spectroscopy of the different areas marked with white dots in Figure 1a. The obtained Raman spectra exhibited typical MoS₂ peaks E_{2g}^1 ($\sim 384 \text{ cm}^{-1}$) and A_{1g} ($\sim 407 \text{ cm}^{-1}$). The observed broadening and shifts of the distance between E_{2g}^1 and A_{1g} Raman modes in the spectra in Figure 1b indicated an increase in MoS₂ thickness, consistent with the previously reported results [51].

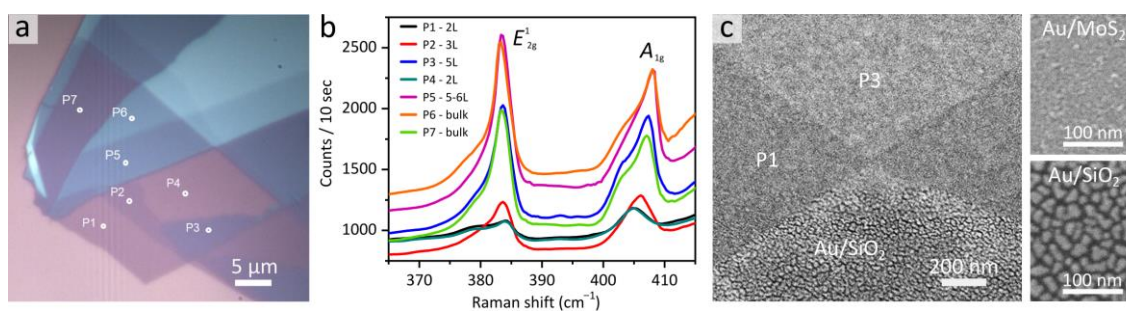


Figure 1. Optical microscopy (a) and Raman characterization (b) of a typical transferred few-layer MoS₂ flake on the SiO₂/Si substrate. Various colors in the optical image are attributed to different thicknesses of MoS₂, i.e., 2 L, 3 L, and thicker MoS₂ layers. The Raman spectra with a 632.8 nm excitation laser were collected from a spot size of about $1 \mu\text{m}$ at each measurement point at n -layered MoS₂. (c) SEM image of the area across the Au/SiO₂-Au/MoS₂ flake surface boundary after deposition of a 4-nm-thick Au film, small SEM images represent the surface morphology of gold on MoS₂ and SiO₂.

To demonstrate the drastic difference in the morphology of Au film on MoS₂ and SiO₂ underlayers, a SEM image of the boundary between Au/MoS₂ and Au/SiO₂ was recorded (see Figures 1c and A1). Clearly, ultrathin gold films on MoS₂ are continuous and without voids, while ultrathin gold films on SiO₂ are composed of particles separated by voids. A similar difference in the morphology of gold on MoS₂ and SiO₂ was previously observed for gold films on MoS₂ monolayers grown by chemical vapor deposition (CVD) [22]. As

can be seen, microscopy images show no visible variation in the morphology of Au grown on the different terraces of MoS₂.

After the metal deposition, the surface morphology of the Au films grown on few-layer MoS₂ was further examined via SEM and AFM. As seen in Figure 2, both the SEM (a–c) and AFM (d–f) images indicate that 4–10-nm-thick Au films on few-layer MoS₂ fully cover the substrate. The polycrystalline structure of Au films was confirmed via SEM images as in Figure 2a–c. The full area metal coverage is due to a low percolation threshold and high density of nucleation sites at the initial stage of the film growth on MoS₂. AFM surface analysis demonstrated in Figure 2d–f revealed an atomically smooth surface with a root-mean-square (RMS) roughness below 0.37 nm for all considered thicknesses, which additionally confirms full substrate coverage by the gold film. At the same time, surface roughness slightly increases with the increase in gold layer thickness, which is typical for continuous polycrystalline Au films [52,53].

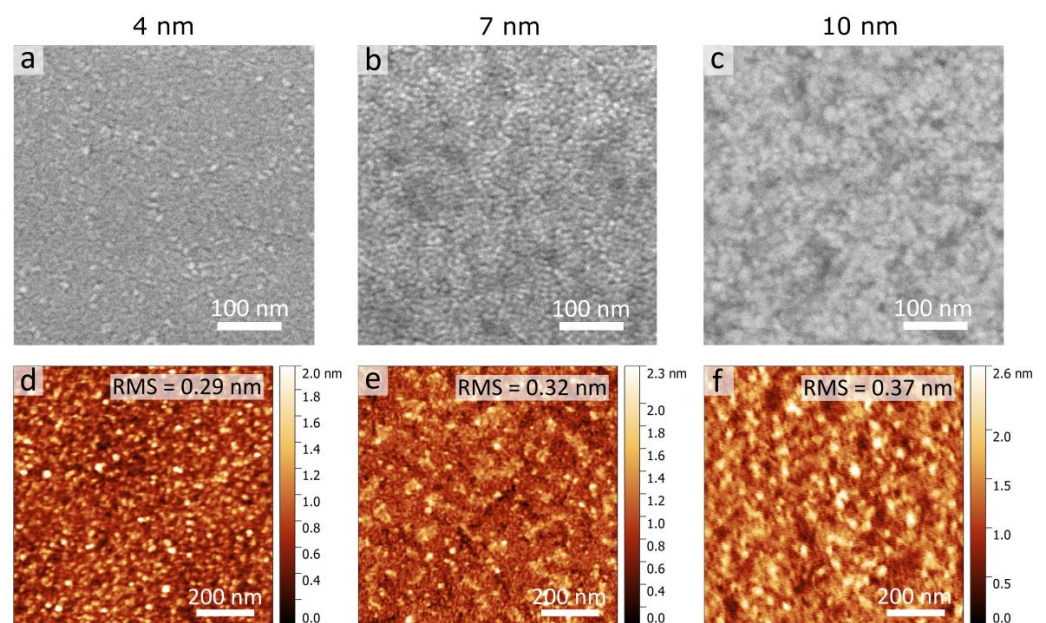


Figure 2. SEM surface images (a–c) and AFM topography scans (d–f) of Au films of varying thickness on few-layer MoS₂ flakes. Values of RMS surface roughnesses of the Au films are indicated within AFM images. The AFM scan area is $1 \times 1 \mu\text{m}^2$.

To probe the local optical response of gold films, we performed s-SNOM microscopy. For the measurements, we chose areas that include the boundary between Au/SiO₂ and Au/MoS₂ which allowed us to visualize the contrast between the optical properties of different gold films. Moreover, we focused on monolayer MoS₂ underlayers rather than multilayer MoS₂ to minimize the influence of MoS₂ on the s-SNOM amplitude. The s-SNOM scans of the boundary between Au/MoS₂ and Au/SiO₂ for Au layer thicknesses of 4, 7 and 10 nm are demonstrated in Figure 3a–c. Here, the near-field amplitude showed a high contrast between Au films grown on the MoS₂ and SiO₂ surface for all thicknesses, with an s-SNOM amplitude at the area of Au/MoS₂ being significantly higher than that for discontinuous film Au/SiO₂. Furthermore, the contrast between Au/MoS₂ and Au/SiO₂ grows with the increase in the gold thickness, starting from about 50% for 4-nm-thick films (Figure 3a) to an order of magnitude for 10-nm-thick films (Figure 3c).

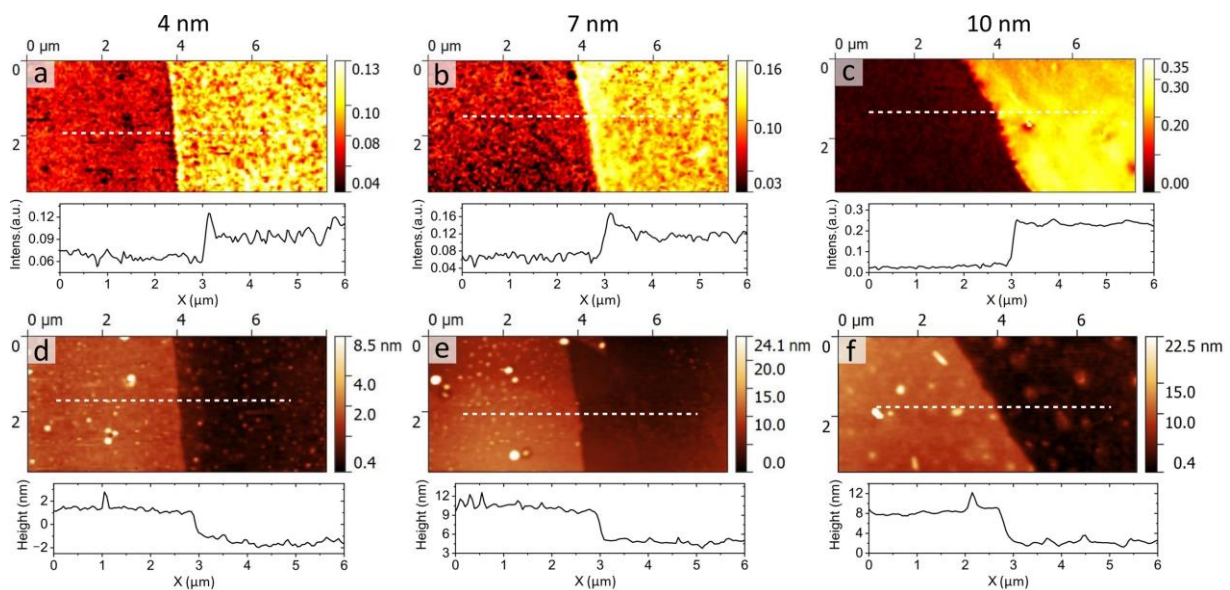


Figure 3. The measured s-SNOM amplitude scans (a–c) across the boundary between Au/SiO₂ and Au/MoS₂ areas for three different thicknesses with the intensity of signal cross-sections, related to the dotted white line, in arbitrary units below and corresponding scans of AFM topography (d–f) with height profiles below.

Higher quality of Au/MoS₂ films on CVD MoS₂ was previously established by the far-field measurements [22] and is qualitatively evident from Figure 1c. Nevertheless, for the additional confirmation we analyzed topography scans presented in Figure 3d–f. We clearly see the existence of a 3–5-nm-high step on the boundary between Au/SiO₂ and Au/MoS₂, in agreement with the previous AFM measurements [20]. Such a difference in thickness can be explained by the higher porosity of Au/SiO₂ films which makes the total volume of Au/SiO₂ film higher than that of Au/MoS₂ film despite the same quantity of metal per unit area being deposited on each substrate. Interestingly, there are correlations between the topography and amplitude maps; for example, some bright spots on the left side of Figure 3d,e turn into dark spots in Figure 3a,b. Moreover, the fluctuation of the near-field amplitude of Au/MoS₂ films grows from $16.8 \cdot 10^{-3}$ to $21.5 \cdot 10^{-3}$ as their thickness increases. Similar behavior is observed for topography scans that show the increase in the surface roughness of Au/MoS₂ from 0.29 to 0.37 nm (Figure 2d–f). These results suggest that the near-field amplitude represents the local optical properties and morphology of gold films, in the spirit of the seminal work [45].

Apart from local optical response distribution, s-SNOM could give additional information about ultrathin film properties as a whole. Indeed, the s-SNOM signal on the surface of the metal depends not only on the scattering properties of the SNOM tip and a sample area immediately underneath it but also on the guided SPP waves that can be excited by the tip and propagate up to dozens of micrometers along the film. The excitation of guided SPP is detectable via near-field fringes typically visible near the line cracks and other defects. Interestingly, despite the straight-line boundary between Au/MoS₂ and Au/SiO₂, no interference fringes are visible in Figure 3a,b. By contrast, a large $10 \times 10 \mu\text{m}^2$ area scan of 10-nm-thick Au/MoS₂ film reveals a line defect and a fringe pattern around it (see Figure 4a). These fringes clearly indicate the capability of the Au/MoS₂ film to guide SPP waves. At the same time, the absence of fringes in Figure 3a–c can be related to the porous nature of Au/SiO₂ film. Below the percolation threshold, the propagation of SPP waves can occur due to the dipole-dipole coupling between adjacent metallic islands, while above the percolation threshold the SPP wave is scattered by the disordered voids in the metal film. As a result, in both cases the phase coherence of SPP waves is rapidly lost,

which, combined with the local fluctuations of optical properties, produces noisy amplitude maps in Figure 3a,b.

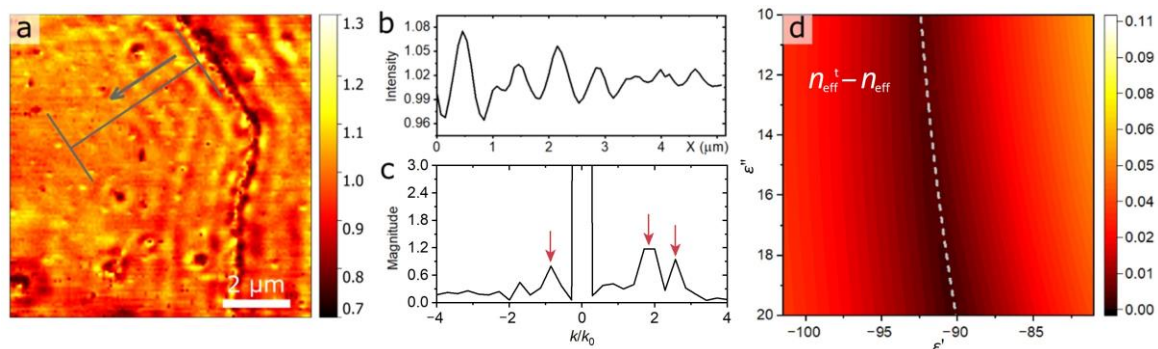


Figure 4. (a) s-SNOM amplitude imaging of fringes observed on 10-nm-thick Au film on MoS₂ near the line-crack edge. (b) Signal profile line scan of the fringes extracted from (a) and averaged over 2.5 μm (gray line in a). (c) FT near-field amplitude of the near-field signal along propagation in (b). (d) Results of ε' and ε'' range determination by comparison of the calculated effective mode index (n_{eff}^t) with the experimentally determined one.

Next, using the capabilities of our s-SNOM setup to measure both the amplitude and phase of the near-field signal, we analyze them to retrieve an effective-mode index of propagation of surface plasmon modes. We carried out a one-dimensional complex Fourier transformation (FT) of the averaged s-SNOM signal along the SPP propagation, as illustrated in Figure 4a by the arrow, which allowed us to extract effective mode indices. As indicated in Figure 4c (the red arrows), the Fourier spectrum has three peaks $k/k_0 \approx 1.87, 2.56$ and -0.85 ; due to the geometry of the reflection mode s-SNOM setup, the “real” values k/k_0 of the modes are shifted from the k/k_0 observable in the experiment [54]. The value of the shift can be expressed as:

$$\beta_0 = k_R + k_0 \cdot \cos \alpha \cdot \sin \beta \quad \beta_0/k_0 = k_R/k_0 + \cos \alpha \cdot \sin \beta, \quad (1)$$

$$\beta_0 = k_L - k_0 \cdot \cos \alpha \cdot \sin \beta \quad \beta_0/k_0 = k_L/k_0 - \cos \alpha \cdot \sin \beta, \quad (2)$$

where β_0 corresponds to the observable mode, k_R/k_0 stays for the “real” effective mode index for the modes on the right side of the Fourier transform, k_L/k_0 for the left side, α is the angle between the wave vector of the incident light and its projection on the sample surface and β is the angle between the projection of the wave vector and the crack from which the light scatters. In our case, the shift is 0.86 due to the geometry of the experimental setup. According to Equations (1) and (2), we observe two propagating modes in the Fourier spectrum: one with effective-mode index 1.71 ($\beta_0/k_0 \approx 2.56$ and $\beta_0/k_0 \approx -0.85$) and the other with 1.02 ($\beta_0/k_0 \approx 1.87$). The latter propagates along the air/Au interface ($k/k_0 \approx 1.02$) while the former along the interface between Au and the substrate ($k/k_0 \approx 1.71$).

In addition, we verified experimental effective-mode indexes by finding the film dielectric constants ε' and ε'' via comparison of experimentally determined n_{eff} with theoretically calculated n_{eff}^t . For this, we performed full-wave electromagnetic simulations using COMSOL Multiphysics to obtain n_{eff}^t selecting different values of dielectric functions ε' and ε'' of 10-nm-thick gold film at a single wavelength of $\lambda = 1550$ nm. Results of the calculated difference $n_{\text{eff}}^t - n_{\text{eff}}$ are presented in Figure 4d. Here, the darker the color of the map, the closer the modes that are obtained for the ε' and ε'' data are to the effective mode indices that are observed in the experiment. It is seen that the effective mode index mainly depends on ε'. At the same time, ε'' is responsible for propagation losses, which are difficult to determine from s-SNOM map, thus can be varied within a reasonable range. From Figure 4d, the ranges for the dielectric function of gold are

$|\epsilon'| = 90\text{--}92.5$, $\epsilon'' = 10\text{--}20$ (darkest areas in Figure 4d indicated by the white dotted line) which is in agreement with the formerly measured dielectric constants $\epsilon' = -95.3$ and $\epsilon'' = 14.5$ at $\lambda = 1550$ nm of 9-nm-thick gold film grown on MoS₂-CVD monolayer [22]. To sum up, the high quality of Au/MoS₂ films was demonstrated by s-SNOM image contrast measurements in Figure 3c, SEM in Figure 2, and by the observation of SPP fringes in Figure 4a. Also, we determined the effective index of SPPs propagating along the 10-nm-thick gold film, and, based on it, extracted the effective values of ϵ' and ϵ'' of the gold film, which agree with the previous measurements.

4. Conclusions

We studied morphology and local optical response of ultrathin gold films deposited on SiO₂ and 2D MoS₂ crystal layers. The results demonstrate the significant contrast in s-SNOM amplitude between Au films on MoS₂ and SiO₂ for all measured thicknesses. As was observed, strong contrast in the s-SNOM signal is related to the different surface morphology and continuity of Au films deposited on SiO₂ and MoS₂ surfaces, which correlates well with the previously reported far-field and near-field investigations. Furthermore, we detected SPP wave propagation at the telecom wavelength range via s-SNOM imaging of near-field fringes from edge defect in 10-nm-thick Au film on MoS₂, and theoretically calculated possible dielectric permittivities of gold. The observation of SPP propagation additionally confirms the high quality of the obtained ultrathin films. As a result, by obtaining nanoscale optical images, we demonstrated s-SNOM to be an effective method for analysis of the structural quality and optical response, which can give information about the propagation of surface waves in ultrathin metal films. We believe that our research will encourage the future use and deep theoretical study of s-SNOM for advanced nanoscale optical characterization of the optical and structural performance of metal-2D material interfaces.

Author Contributions: D.I.Y., D.V.G., G.A.E., A.A.V., A.V.A. and V.S.V. proposed the concept, conceived and designed the experiments and wrote original draft. D.I.Y., D.V.G., M.S.M. and S.M.N. performed the measurements and analyzed the data. D.V.G. and A.A.V. provided theoretical support. All authors discussed the results and contributed to manuscript preparation. All authors have read and agreed to the published version of the manuscript.

Funding: The work was supported by the Russian Science Foundation, grant No. 21-72-10163.

Data Availability Statement: The data presented in this study are available on request from the corresponding author.

Acknowledgments: The authors gratefully acknowledge Yuri Stebunov for providing excellent technical assistance with the mechanical exfoliation technique. The authors thank the MIPT's Shared Research Facilities Center for the use of their equipment.

Conflicts of Interest: The authors declare no conflict of interest.

Appendix A

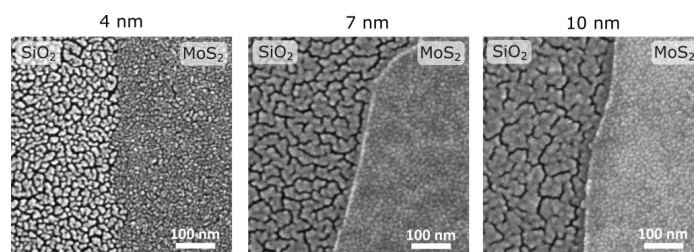


Figure A1. The comparison SEM images for gold films grown on SiO₂ and MoS₂ for 4 nm, 7 nm, and 10 nm film thickness.

References

1. Bi, Y.-G.; Liu, Y.-F.; Zhang, X.-L.; Yin, D.; Wang, W.-Q.; Feng, J.; Sun, H.-B. Ultrathin Metal Films as the Transparent Electrode in ITO-Free Organic Optoelectronic Devices. *Adv. Opt. Mater.* **2019**, *7*, 1800778. [[CrossRef](#)]
2. Malureanu, R.; Lavrinenko, A. Ultra-thin films for plasmonics: A technology overview. *Nanotechnol. Rev.* **2015**, *4*, 259–275. [[CrossRef](#)]
3. Maniyara, R.A.; Rodrigo, D.; Yu, R.; Canet-Ferrer, J.; Ghosh, D.S.; Yongsunthon, R.; Pruneri, V. Tunable plasmons in ultrathin metal films. *Nat. Photonics* **2019**, *13*, 328–333. [[CrossRef](#)]
4. Yun, J. Ultrathin Metal films for Transparent Electrodes of Flexible Optoelectronic Devices. *Adv. Funct. Mater.* **2017**, *27*, 1606641. [[CrossRef](#)]
5. Bi, Y.-G.; Feng, J.; Ji, J.-H.; Chen, Y.; Liu, Y.-S.; Li, Y.-F.; Liu, Y.-F.; Zhang, X.-L.; Sun, H.-B. Ultrathin and ultrasmooth Au films as transparent electrodes in ITO-free organic light-emitting devices. *Nanoscale* **2016**, *8*, 10010–10015. [[CrossRef](#)]
6. Sukham, J.; Takayama, O.; Lavrinenko, A.V.; Malureanu, R. High-Quality Ultrathin Gold Layers with an APTMS Adhesion for Optimal Performance of Surface Plasmon Polariton-Based Devices. *ACS Appl. Mater. Interfaces* **2017**, *9*, 25049–25056. [[CrossRef](#)]
7. Kossoy, A.; Merk, V.; Simakov, D.; Leosson, K.; Kéna-Cohen, S.; Maier, S.A. Optical and Structural Properties of Ultra-thin Gold Films. *Adv. Opt. Mater.* **2015**, *3*, 71–77. [[CrossRef](#)]
8. Huo, P.; Zhang, S.; Liang, Y.; Lu, Y.; Xu, T. Hyperbolic Metamaterials and Metasurfaces: Fundamentals and Applications. *Adv. Opt. Mater.* **2019**, *7*, 1801616. [[CrossRef](#)]
9. Petrov, I.; Barna, P.B.; Hultman, L.; Greene, J.E. Microstructural evolution during film growth. *J. Vac. Sci. Technol.* **2003**, *21*, S117. [[CrossRef](#)]
10. Abd El-Fattah, Z.M.; Mkhitarian, V.; Brede, J.; Fernández, L.; Li, C.; Guo, Q.; Ghosh, A.; Echarri, A.R.; Naveh, D.; Xia, F.; et al. Plasmonics in Atomically Thin Crystalline Silver Films. *ACS Nano* **2019**, *13*, 7771–7779. [[CrossRef](#)]
11. Logeeswaran, V.J.; Kobayashi, N.P.; Islam, M.S.; Wu, W.; Chaturvedi, P.; Fang, N.X.; Wang, S.Y.; Williams, R.S. Ultrasmooth Silver Thin Films Deposited with a Germanium Nucleation Layer. *Nano Lett.* **2009**, *9*, 178–182. [[CrossRef](#)]
12. Zaretski, A.V.; Root, S.E.; Savchenko, A.; Molokanova, E.; Printz, A.D.; Jibril, L.; Arya, G.; Mercola, M.; Lipomi, D.J. Metallic Nanoislands on Graphene as Highly Sensitive Transducers of Mechanical, Biological, and Optical Signals. *Nano Lett.* **2016**, *16*, 1375–1380. [[CrossRef](#)]
13. Gong, C.; Huang, C.; Miller, J.; Cheng, L.; Hao, Y.; Cobden, D.; Kim, J.; Ruoff, R.S.; Wallace, R.M.; Cho, K.; et al. Metal Contacts on Physical Vapor Deposited Monolayer MoS₂. *ACS Nano* **2013**, *7*, 11350–11357. [[CrossRef](#)]
14. Huang, Y.; Pan, Y.H.; Yang, R.; Bao, L.H.; Meng, L.; Luo, H.L.; Gao, H.J. Universal mechanical exfoliation of large-area 2D crystals. *Nat. Commun.* **2020**, *11*, 2453. [[CrossRef](#)] [[PubMed](#)]
15. Sarkar, D.; Liu, W.; Xie, X.; Anselmo, A.C.; Mitragotri, S.; Banerjee, K. MoS₂ Field-Effect Transistor for Next-Generation Label-Free Biosensors. *ACS Nano* **2014**, *8*, 3992–4003. [[CrossRef](#)]
16. Lopez-Sanchez, O.; Lembke, D.; Kayci, M.; Radenovic, A.; Kis, A. Ultrasensitive photodetectors based on monolayer MoS₂. *Nat. Nanotech.* **2013**, *8*, 497–501. [[CrossRef](#)]
17. Tsai, M.-L.; Su, S.-H.; Chang, J.-K.; Tsai, D.-S.; Chen, C.-H.; Wu, C.-I.; Li, L.-J.; Chen, L.-J.; He, J.-H. Monolayer MoS₂ Heterojunction Solar Cells. *ACS Nano* **2014**, *8*, 8317–8322. [[CrossRef](#)] [[PubMed](#)]
18. Popov, I.; Seifert, G.; Tománek, D. Designing Electrical Contacts to MoS₂ Monolayers: A Computational Study. *Phys. Rev. Lett.* **2012**, *108*, 156802. [[CrossRef](#)] [[PubMed](#)]
19. Yuan, H.; Cheng, G.; You, L.; Li, H.; Zhu, H.; Li, W.; Kopanski, J.J.; Obeng, Y.S.; Walker, A.R.H.; Gundlach, D.J.; et al. Influence of Metal–MoS₂ Interface on MoS₂ Transistor Performance: Comparison of Ag and Ti Contacts. *ACS Appl. Mater. Interfaces* **2015**, *7*, 2. [[CrossRef](#)]
20. Shen, Y.-H.; Hsu, C.-C.; Chang, P.-C.; Lin, W.-C. Height reversal in Au coverage on MoS₂ flakes/SiO₂: Thermal control of interfacial nucleation. *Appl. Phys. Lett.* **2019**, *114*, 181601. [[CrossRef](#)]
21. Kidd, T.E.; Weber, J.; O’Leary, E.; Stollenwerk, A.J. Preparation of Ultrathin Gold Films with Subatomic Surface Roughness. *Langmuir* **2021**, *37*, 9472–9477. [[CrossRef](#)] [[PubMed](#)]
22. Yakubovsky, D.I.; Stebunov, Y.V.; Kirtaev, R.V.; Ermolaev, G.A.; Mironov, M.S.; Novikov, S.M.; Arsenin, A.V.; Volkov, V.S. Ultrathin and Ultrasmooth Gold Films on Monolayer MoS₂. *Adv. Mater. Interfaces* **2019**, *6*, 1900196. [[CrossRef](#)]
23. Zhou, H.; Yu, F.; Guo, C.F.; Wang, Z.; Lan, Y.; Wang, G.; Fang, Z.; Liu, Y.; Chen, S.; Sun, L.; et al. Well-oriented epitaxial gold nanotriangles and bowties on MoS₂ for surface-enhanced Raman scattering. *Nanoscale* **2015**, *7*, 9153–9157. [[CrossRef](#)]
24. Sun, Y.; Zhao, H.; Zhou, D.; Zhu, Y.; Ye, H.; Moe, Y.A.; Wang, R. Direct observation of epitaxial alignment of Au on MoS₂ at atomic resolution. *Nano Res.* **2019**, *12*, 947–954. [[CrossRef](#)]
25. Chen, K.-C.; Lai, S.-M.; Wu, B.-Y.; Chen, C.; Lin, S.-Y. Van der Waals Epitaxy of Large-Area and Single-Crystalline Gold Films on MoS₂ for Low-Contact-Resistance 2D–3D Interfaces. *ACS Appl. Nano Mater.* **2020**, *3*, 2997–3003. [[CrossRef](#)]
26. Lu, J.; Lu, J.H.; Liu, H.; Liu, B.; Gong, L.; Tok, E.S.; Loh, K.P.; Sow, C.H. Microlandscaping of Au Nanoparticles on Few-Layer MoS₂ Films for Chemical Sensing. *Small* **2015**, *11*, 1792–1800. [[CrossRef](#)] [[PubMed](#)]
27. Kidd, T.E.; Weber, J.; Holzapfel, R.; Doore, K.; Stollenwerka, A.J. Three-dimensional quantum size effects on the growth of Au islands on MoS₂. *Appl. Phys. Lett.* **2018**, *113*, 191603. [[CrossRef](#)]

28. Shen, T.; Valencia, D.; Wang, Q.; Wang, K.-C.; Povolotskyi, M.; Kim, M.J.; Klimeck, G.; Chen, Z.; Appenzeller, J. MoS₂ for Enhanced Electrical Performance of Ultrathin Copper Films. *ACS Appl. Mater. Interfaces* **2019**, *11*, 31. [[CrossRef](#)]
29. Zhang, Y.W.; Wu, B.Y.; Chen, K.C.; Wu, C.H.; Lin, S.Y. Highly conductive nanometer-thick gold films grown on molybdenum disulfide surfaces for interconnect applications. *Sci. Rep.* **2020**, *10*, 14463. [[CrossRef](#)]
30. Liu, Y.W.; Zhang, D.J.; Tsai, P.C.; Chiang, C.T.; Tu, W.C.; Lin, S.Y. Nanometer-thick copper films with low resistivity grown on 2D material surfaces. *Sci. Rep.* **2022**, *12*, 1823. [[CrossRef](#)]
31. Shi, Y.; Huang, J.K.; Jin, L.; Hsu, Y.T.; Yu, S.F.; Li, L.J.; Yang, H.Y. Selective Decoration of Au Nanoparticles on Monolayer MoS₂ Single Crystals. *Sci. Rep.* **2013**, *3*, 1839. [[CrossRef](#)] [[PubMed](#)]
32. Miao, J.; Hu, W.; Jing, Y.; Luo, W.; Liao, L.; Pan, A.; Wu, S.; Cheng, J.; Chen, X.; Lu, W. Surface Plasmon-Enhanced Photodetection in Few Layer MoS₂ Phototransistors with Au Nanostructure Arrays. *Small* **2015**, *11*, 2392–2398. [[CrossRef](#)] [[PubMed](#)]
33. Chen, X.; Hu, D.; Mescall, R.; You, G.; Basov, D.N.; Dai, Q.; Liu, M. Modern Scattering-Type Scanning Near-Field Optical Microscopy for Advanced Material Research. *Adv. Mater.* **2019**, *31*, 1804774. [[CrossRef](#)]
34. Zhang, W.; Chen, Y. Visibility of subsurface nanostructures in scattering-type scanning near-field optical microscopy imaging. *Opt. Express* **2020**, *28*, 6696–6707. [[CrossRef](#)] [[PubMed](#)]
35. Bauld, R.; Hesari, M.; Workentin, M.S.; Fanchini, G. Thermal stability of Au₂₅– molecular precursors and nucleation of gold nanoparticles in thermosetting polyimide thin films. *Appl. Phys. Lett.* **2012**, *101*, 243114. [[CrossRef](#)]
36. Stanciu, S.G.; Tranca, D.E.; Zampini, G.; Hristu, R.; Stanciu, G.A.; Chen, X.; Liu, M.; Stenmark, H.A.; Latterini, L. Scattering-type Scanning Near-Field Optical Microscopy of Polymer-Coated Gold Nanoparticles. *ACS Omega* **2022**, *7*, 11353–11362. [[CrossRef](#)]
37. Alonso-González, P.; Nikitin, A.; Gao, Y.; Woessner, A.; Lundberg, M.B.; Principi, A.; Forcellini, N.; Yan, W.; Vélez, S.; Huber, A.J.; et al. Acoustic terahertz graphene plasmons revealed by photocurrent nanoscopy. *Nat. Nanotech.* **2017**, *12*, 31–35. [[CrossRef](#)] [[PubMed](#)]
38. Nikelshparg, E.I.; Baizhumanov, A.A.; Bochkova, Z.V.; Novikov, S.M.; Yakubovsky, D.I.; Arsenin, A.V.; Volkov, V.S.; Goodilin, E.A.; Semenova, A.A.; Sosnovtseva, O.; et al. Detection of hypertension-induced changes in erythrocytes by SERS nanosensors. *Biosensors* **2022**, *12*, 32. [[CrossRef](#)]
39. Brazhe, N.A.; Nikelshparg, E.I.; Baizhumanov, A.A.; Grivennikova, V.G.; Semenova, A.A.; Novikov, S.M.; Volkov, V.S.; Arsenin, A.V.; Yakubovsky, D.I.; Evlyukhin, A.B.; et al. SERS uncovers the link between conformation of cytochrome c heme and mitochondrial membrane potential. *Free. Radic. Biol. Med.* **2023**, *196*, 133–144. [[CrossRef](#)]
40. Ermolaev, G.A.; Grudinin, D.V.; Stebunov, Y.V.; Voronin, K.V.; Kravets, V.G.; Duan, J.; Mazitov, A.B.; Tselikov, G.I.; Bylinkin, A.; Yakubovsky, D.I.; et al. Giant optical anisotropy in transition metal dichalcogenides for next-generation photonics. *Nat. Commun.* **2021**, *12*, 854. [[CrossRef](#)] [[PubMed](#)]
41. Zhang, S.; Li, B.; Chen, X.; Ruta, F.L.; Shao, Y.; Sternbach, A.J.; Basov, D.N. Nano-spectroscopy of excitons in atomically thin transition metal dichalcogenides. *Nat. Commun.* **2022**, *13*, 542. [[CrossRef](#)]
42. Hu, F.; Fei, Z. Recent Progress on Exciton Polaritons in Layered Transition-Metal Dichalcogenides. *Adv. Optical Mater.* **2020**, *8*, 1901003. [[CrossRef](#)]
43. de Oliveira, T.V.A.G.; Nörenberg, T.; Álvarez-Pérez, G.; Wehmeier, L.; Taboada-Gutiérrez, J.; Obst, M.; Hempel, F.; Lee, E.J.H.; Klopff, J.M.; Errea, I.; et al. Nanoscale-Confined Terahertz Polaritons in a van der Waals Crystal. *Adv. Mater.* **2021**, *33*, 2005777. [[CrossRef](#)]
44. Govyadinov, A.A.; Mastel, S.; Golmar, F.; Chuvilin, A.; Carney, P.S.; Hillenbrand, R. Recovery of Permittivity and Depth from Near-Field Data as a Step toward Infrared Nanotomography. *ACS Nano* **2014**, *8*, 6911–6921. [[CrossRef](#)] [[PubMed](#)]
45. Hillenbrand, R.; Keilmann, F. Complex Optical Constants on a Subwavelength Scale. *Phys. Rev. Lett.* **2000**, *85*, 3029–3032. [[CrossRef](#)] [[PubMed](#)]
46. Mastel, S.; Govyadinov, A.A.; Maissen, C.; Chuvilin, A.; Berger, A.; Hillenbrand, R. Understanding the Image Contrast of Material Boundaries in IR Nanoscopy Reaching 5 nm Spatial Resolution. *ACS Photonics* **2018**, *5*, 3372–3378. [[CrossRef](#)]
47. Mester, L.; Govyadinov, A.A.; Hillenbrand, R. High-fidelity nano-FTIR spectroscopy by on-pixel normalization of signal harmonics. *Nanophotonics* **2022**, *11*, 377–390. [[CrossRef](#)]
48. Mastel, S.; Govyadinov, A.A.; de Oliveira, T.V.A.G.; Amenabar, I.; Hillenbrand, R. Nanoscale-resolved chemical identification of thin organic films using infrared near-field spectroscopy and standard Fourier transform infrared references. *Appl. Phys. Lett.* **2015**, *106*, 023113. [[CrossRef](#)]
49. Babicheva, V.E.; Gamage, S.; Stockman, M.I.; Abate, Y. Near-field edge fringes at sharp material boundaries. *Opt. Express* **2017**, *25*, 23935. [[CrossRef](#)]
50. Yakubovsky, D.I.; Arsenin, A.V.; Kirtaev, R.V.; Ermolaev, G.A.; Stebunov, Y.S.; Volkov, V.S. Near-field characterization of ultra-thin metal films. *J. Phys. Conf. Ser.* **2020**, *1461*, 012193. [[CrossRef](#)]
51. Lee, C.; Yan, H.; Bru, L.E.; Heinz, T.F.; Hone, J.; Ryu, S. Anomalous Lattice Vibrations of Single- and Few-Layer MoS₂. *ACS Nano* **2010**, *4*, 2695–2700. [[CrossRef](#)] [[PubMed](#)]
52. Yakubovsky, D.I.; Arsenin, A.V.; Stebunov, Y.V.; Fedyanin, D.Y.; Volkov, V.S. Optical constants and structural properties of thin gold films. *Opt. Express* **2017**, *25*, 25574–25587. [[CrossRef](#)] [[PubMed](#)]

53. Yakubovsky, D.I.; Fedyanin, D.Y.; Arsenin, A.V.; Volkov, V.S. Optical constant of thin gold films: Structural morphology determined optical response. *AIP Conf. Proc.* **2017**, *1874*, 040057.
54. Hu, D.; Yang, X.; Li, C.; Liu, R.; Yao, Z.; Hu, H.; Dai, Q. Probing optical anisotropy of nanometer-thin van der Waals microcrystals by near-field imaging. *Nat. Commun.* **2017**, *8*, 1471. [[CrossRef](#)] [[PubMed](#)]

Disclaimer/Publisher's Note: The statements, opinions and data contained in all publications are solely those of the individual author(s) and contributor(s) and not of MDPI and/or the editor(s). MDPI and/or the editor(s) disclaim responsibility for any injury to people or property resulting from any ideas, methods, instructions or products referred to in the content.